Article:
Kłosowski, MM, Carzaniga, R, Abellan, P et al. (4 more authors) (2017) Electron Microscopy Reveals Structural and Chemical Changes at the Nanometer Scale in the Osteogenesis Imperfecta Murine Pathology. ACS Biomaterials Science & Engineering, 3 (11). pp. 2788-2797. ISSN 2373-9878

https://doi.org/10.1021/acsbiomaterials.6b00300

Electron microscopy reveals structural and chemical changes at the nanometre scale in the osteogenesis imperfecta murine pathology

Authors:

Michał M. Kłosowski[1], Raffaella Carzaniga[2], Patricia Abellan[3], Quentin Ramasse[3], David W. McComb[4], Alexandra E. Porter[1], Sandra J. Shefelbine[5]

[1]Imperial College London, Department of Materials and Engineering, Imperial College London, Royal School of Mines, South Kensington Campus, London, SW7 2AZ, UK

[2]Cancer Research UK, Francis Crick Institute, 44 Lincoln's Inn Fields, London, WC2A 3LY, UK

[3]SuperSTEM Laboratory, SciTech Daresbury Campus, Keckwick Lane, Daresbury, Warrington, WA4 4AD, UK

[4]The Ohio State University, Department of Materials Science and Engineering, Center for Electron Microscopy and Analysis, 1305 Kinnear Road,Columbus, OH 43212, USA

[5]Northeastern University, Department of Mechanical and Industrial Engineering, 334 Snell Engineering Center, Northeastern University, 360 Huntington Ave, Boston, MA 02115, USA

Corresponding Authors: Sandra J. Shefelbine, Northeastern University, Department of Mechanical and Industrial Engineering, 334 Snell Engineering Center, Northeastern University, 360 Huntington Ave, Boston, MA 02115, USA; phone: +1-617-373-3199 ; e-mail: s.shefelbine@neu.edu

Alexandra E. Porter, Imperial College London, Department of Materials and Engineering, Royal School of Mines, South Kensington Campus, London, SW7 2AZ, UK; phone: (+44)207594 9691; e-mail: a.porter@imperial.ac.uk

David W. McComb, The Ohio State University, Department of Materials Science and Engineering, Center for Electron Microscopy and Analysis, 1305 Kinnear Road,Columbus, OH 43212, USA; phone: +1-614-643-3462; e-mail: mccomb.29@osu.edu

Abstract

Alternations of collagen and mineral at the molecular level may have a significant impact on the strength and toughness of bone. In this study, scanning transmission electron microscopy (STEM) and electron energy-loss spectroscopy (EELS) were employed to study structural and compositional changes in bone pathology at nanometer spatial resolution. Tail tendon and femoral bone of osteogenesis imperfecta murine (oim – brittle bone disease) and wild type (WT) mice were compared to reveal defects in the architecture and chemistry of the collagen and collagen-mineral composite in the oim tissue at the molecular level. There were marked differences in the sub-structure and organization of the collagen fibrils in oim tail

tendon; some regions have clear fibril banding and organization, while in other regions fibrils are disorganized. Malformed collagen fibrils were loosely packed, often bent and devoid of banding pattern. In bone, differences were detected in the chemical composition of mineral in oim and WT. While mineral present in WT and oim bone exhibited the major characteristics of apatite, examination in EELS of the fine structure of the carbon K ionisation edge revealed a significant variation in the presence of carbonate in different regions of bone. Variations have been also observed in the fine structure and peak intensities of the nitrogen K-edge. These alterations are suggestive of differences in the maturation of collagen nucleation sites or crosslinks. Future studies will aim to establish the scale and impact of the modifications observed in oim tissues. The compositional and structural alterations at the molecular level cause deficiencies at larger length scales. Understanding the effect of molecular alterations to pathologic bone is critical to the design of effective therapeutics.

Keywords:

EELS, STEM, electron microscopy, matrix mineralization, collagen, osteogenesis imperfecta

1. Introduction

Osteogenesis imperfecta (OI or brittle bone disease) is a genetic, inherited disorder, which affects nearly 1 in 10,000 people worldwide.[1] Brittle bone disease is caused by a mutation in the genes coding for type I collagen. Changes in OI collagen are associated with alteration of genes responsible for α_1 and α_2 chain expression, usually caused by a point substitution of one amino acid. There are over 1500 mutations causing changes in the structure or quantity of collagen.[2] Disruption in type I collagen affects collagen-based tissue and results in skeletal fragility and spontaneous fractures. Pathological changes are not limited to bone. Other common consequences of OI are impaired tendons, blue sclera, dentogenesis and loose joints.[1] Severe mutations may even result in antenatal death.

Moderate to severe phenotypes of human OI are mimicked in the mouse model of OI, osteogenesis imperfecta murine (oim)[3] In oim, the natural triple-helix of two α_1 and one α_2 chains is replaced by a homotrimer of three α_1 chains.[3] This alteration results in an increase in intermolecular separation.[4,5] Due to poor packing, oim collagen fibrils bend and twist easily causing disruption in the tissue organization.[6] This hypothesis has been supported by X-ray diffraction[7] and by a molecular modelling of the oim mouse defects[8], showing loss of lateral packing of collagen. However, oim collagen fibrils seem to retain their banded structure.[7,9]

Not only is collagen fibril organization changed in OI, but the interaction interface between the mineral and collagen is also affected.[6] Overexpression of $^{-}$OH groups and sugar side groups of amino acids in oim tissue was suggested by chromatography studies.[2,10,11] These phenomena may be related to changes in collagen crosslinking, which potentially has an impact on the mineralization process. A decrease in the number of enzymatic crosslinks[12] and an increase in the number of non-enzymatic crosslinks were observed in oim model.[13] Additional changes have also been observed in the expression of non-collagenous proteins (NCP) in affected tissues.[11,14]

Previous studies have demonstrated a strong relationship between the overall strength of the material and the orientation and morphology of the mineral crystals. In OI tissues, the long axes of crystals exhibit a deviation from their alignment parallel to collagen fibrils[15,16] and a great variation in the shape and size of the apatite crystals is observed.[6] The mineral crystals are smaller, more randomly aligned and distributed in OI bone, compared to healthy bone.[6,15–19] There also have been reports about the formation of large bulky crystals and the

aggregation of small crystals seen in oim.[6,19,20] These reports are not contradictory. The presence and organization of small crystals was assessed mainly by small-angle X-ray scattering (SAXS), which is not optimal for detection of structures larger than 50 nm.[19] Hence, there could be two groups of crystals: small crystals seen in intra-fibrillar regions, and large crystals encountered in extra-fibrillar regions.[19] Computational models suggested that the morphology of the apatite crystals have a greater impact on the mechanical behaviour of bone than the destabilized collagen fibrils.[21]

The mineral in OI tissues tends to have a lower degree of carbonate content (measured by bulk FTIR and Raman spectroscopy)[13,16] and reduced crystallinity (measured by bulk XRD).[22] It was proposed that in the bones of oim mice, high remodelling rates result in less mature crystals and therefore less carbonate substitution.[23] In contrast, a different model of the OI disease (BrtlIV) exhibits an increase in the carbonate content measured by Raman spectroscopy.[24] Generally, the relationship between the remodelling rates and the crystallinity and chemistry of mineral is not fully understood and often controversial.[25]

The majority of studies on OI bone have been conducted at the whole bone and tissue levels and very little research has been conducted at the fibril levels to relate directly how changes in the molecular composition and structure of collagen fibrils alter mineralization. This deficiency in our knowledge has arisen due to the challenge of applying appropriate techniques to provide spatially resolved information about the mineral and collagen at this length scale. In particular, very few techniques are available to directly probe spatially-resolved chemical information at the nanometre scale. Analytical electron microscopy is currently the only method available that can provide maps of the distribution of mineral and collagen chemistry with this resolution.[26] However, accurate nano-scale analysis of bone is extremely challenging due to the its susceptibility to radiation. Low electron doses are often insufficient to obtain spectral information with optimal spatial and energy resolution and signal-to-noise ratio. . In addition, it is vital to preserve the chemistry and structure of the tissue during sample preparation to analyse the sample in its near-native state. In this paper, we combine a sample-preparation method that simultaneously preserves mineral, ions, and the collagen fibrils with nano-analytical electron microscopy at electron doses carefully controlled to avoid radiation-induced artefacts. We used transmission electron microscopy to examine the nano-structure of mineralized fibrils in bone and non-mineralized fibrils from

tail tendon and electron energy-loss spectroscopy (EELS) to identify compositional differences between oim and WT tissues.

2. Materials and methods

Mice were obtained with local and Home Office approval, euthanized with carbon dioxide and dissected. Bone samples were obtained from 3 femurs of 8 week old oim (oim/oim -/-) and wild type (oim/oim +/+) mice. Non-mineralized tail tendon collagen was harvested from mouse tails. Tails were dissected and tendons were cut and gently pulled out with a surgical needle and tweezers. Small pieces of mid-shaft cortical bone and tail tendon were cut with a scalpel blade and fitted into 200µm-deep flat specimen carriers for cryo-fixation. Both tissues were prepared using high pressure freezing/freeze-substitution (HPF/FS) methods as described elsewhere. [27]

Rapid cryofixation under high pressure of 200µm-thick samples was performed in a Leica EMPACT2 (Leica Microsystems, Vienna) apparatus with 1-hexadecene used as a cryo-preservative. The freeze-substitution with acetone cocktail was performed in a Leica EM AFS2 apparatus at -90°C. For bones, an acetone cocktail of 3% glutaraldehyde was used. For tendons, the acetone cocktail was enhanced with 0.5% osmium tetroxide. After 8h, the temperature started to rise gradually, until it reached 0°C in 18h. Two 15min acetone washes were performed on the samples, before they reached room temperature.

Osmium tetroxide is a strong oxidising agent, which reacts with specific functional groups in the collagen chain, e.g. unsaturated carbon-carbon bonds, carbonyl and amide groups. Since the coordination environment of these functional groups would be altered, stained samples were not used for chemical analysis.

Samples were immersed successively in 1:3, 1:1 and 3:1 resin:acetone solutions for 24h each. The resin was prepared from a mixture of 2.6ml of Quetol651, 3.8ml of nonenylsuccinic anhydride (NSA), 1.3ml of methylnadic anhydride (MNA) and 0.2ml of benzyldimethylamine (BDMA), (Agar Scientific, Dorset, UK). Next, daily changes of pure resin were performed for 7 days to ensure full infiltration of samples. During this process the samples were kept under vacuum. After eight days, the samples were cured in the oven at 60°C for 48h under vacuum. Although hydrated collagen denatures at ~60°C, dehydrated collagen remains stable when heated up to ~160°C.[28] Therefore, curing should not alter the

structure and chemistry of the samples. Ultrathin (70nm) sections of bone and tendon samples were cut with an ultramicrotome.

There were several electron microscopy techniques used in the present study: bright-field transmission electron microscopy (BF-TEM), selected area electron diffraction (SAED), scanning transmission electron microscopy (STEM) in annular dark field mode (ADF-STEM) and electron energy-loss spectroscopy (EELS). An overview of electron microscopy methods for the examination of mineralizing tissues can be found elsewhere.[27]

BF-TEM and SAED of mouse bone and tendon were performed on JEOL2000FX and FEI Titan instruments operated at 200kV and 300kV, respectively.

We used different TEMs to obtain the optimal spatial and energy resolution at minimal doses. Although we were able to obtain the highest energy resolution on the Titan TEM at Ohio State University, the electron doses were similar on all microscopes. Total electron doses were kept below 10^4 electrons/nm^2 to minimize radiation damage. The dose rate was 10^3 electrons/nm^2 per second. Tomographic studies of the collagen fibrils used doses of up to 7100 e/nm^2,[29,30] which are close to the limit for radiation damage. Sub-pixel scanning was used during the acquisition of spectrum images (whereby the beam is rastered across a defined area of the sample, acquiring a spectrum at each step) to further minimize localized beam damage during spectral images collection.

The collagen samples are most likely to undergo radiolysis and the mineral could undergo a mixture of radiolysis and knock-on damage.[31] In the bone samples, radiolysis damage may result in changes to EELS spectra of carbon, nitrogen and oxygen edges.[26,32] We carefully monitored the fine structure at each edge of the spectra being acquired for any signs of the damage. Importantly, we used features in the carbon (~286eV) and oxygen (~530eV) k-edge as damage markers. Only spectra, which did not show changes characteristic of damage, were analysed.

For non-monochromated STEM-EELS, a C_s (image-)corrected, FEI Titan 80-300 microscope fitted with a Gatan Tridem spectrometer was used (Imperial College, UK). An optimal signal-to-noise ratio was achieved using a probe convergence semi-angle of 8mrad (a 50mm condenser aperture, a spot size 9, beam current 5-20pA). Using a 48mm camera length, the ADF-STEM collection semi-angle range is 33-181mrad and the EELS collection semi-angle is 14mrad. The full-width at half-maximum (FWHM) of the non-monochromated zero loss

peak (ZLP) was 0.6-0.7eV. Spectral images were collected from regions of interest with the energy dispersion of 0.05 eV/channel. Spectra of individual pixels were added up to reduce noise.

For monochromated STEM-EELS, a C_s (image-)corrected, FEI Titan^3 60-300 microscope with a Gatan Quantum spectrometer was used (Ohio State University, USA). The same beam current, convergence and collection semi-angles were used as above. The FWHM of the monochromated ZLP was 0.3-0.5eV.

Additional monochromated STEM-EELS experiments were carried out using a Nion UltraSTEM100MC microscope operated at 100kV (SuperSTEM Lab, Daresbury). The HAADF collection semi-angle range was 85-190 mrad, with an EELS collection semi-angle of 44 mrad. The FWHM of the monochromated ZLP was 0.05-0.06eV, although a dispersion of 0.1 eV/channel was chosen to provide a large enough energy range to record the detailed fine structure of the carbon K and nitrogen K edges, resulting in an effective energy resolution (limited by the spectrometer CCD point spread function) of approximately 0.3eV. Reducing the incoming beam current to 9pA resulted in electron doses below 10^4 electrons/nm^2, comparable to those used on the Titan microscopes. Prior to imaging, samples were baked for 12h in a vacuum oven (10^{-6} Torr) with a rising temperature gradient (from room temperature to 100°C) with a total time of 6 hours, followed by a steady-state temperature plateau of 50°C. Baking was used to reduce hydrocarbon contamination.[33]

A power law background subtraction with 30eV window or wider was performed on all acquired edges. Spectra were usually aligned to the first peak and normalized to the most intense peak. Calibration of the spectra was based on the literature (see each edge for details).

All S/TEM observations were made after viewing multiple regions of three different animals in each group (wild type and oim). The significance of our observations was assessed with two-sample two-tailed t-test in Origin (OriginLab, Massachusetts, USA).

3. Results

3.1. Alternations of collagen matrix in tail tendon of oim mice

Tail tendon collagen was used to examine the collagen matrix without any mineral content. The most characteristic feature of collagen fibrils at the nanoscale level of hierarchy is the periodic banding pattern. The periodic segments are typically about 67 nm in length and

consist of two regions of dark and light contrast, corresponding to so-called gap and overlap regions, respectively (Figure 1A). Mass thickness contrast arising from heavy metal staining reveals an additional sub-banding pattern, which corresponds to positively charged regions of the collagen fibril (Figure 1B).[34,35] The composition of the sub-bands is not known, although some of the bands were suggested as mineral nucleation sites.[29] In both, WT and oim collagen, the mature fibrils exhibited this sub-banding pattern (Figure SI1). Comparison of sub-banding features in WT and oim tendon did not show any significant differences at the 0.05 levelin the length of the gap, overlap and full period of the collagen fibrils (Table SI1).

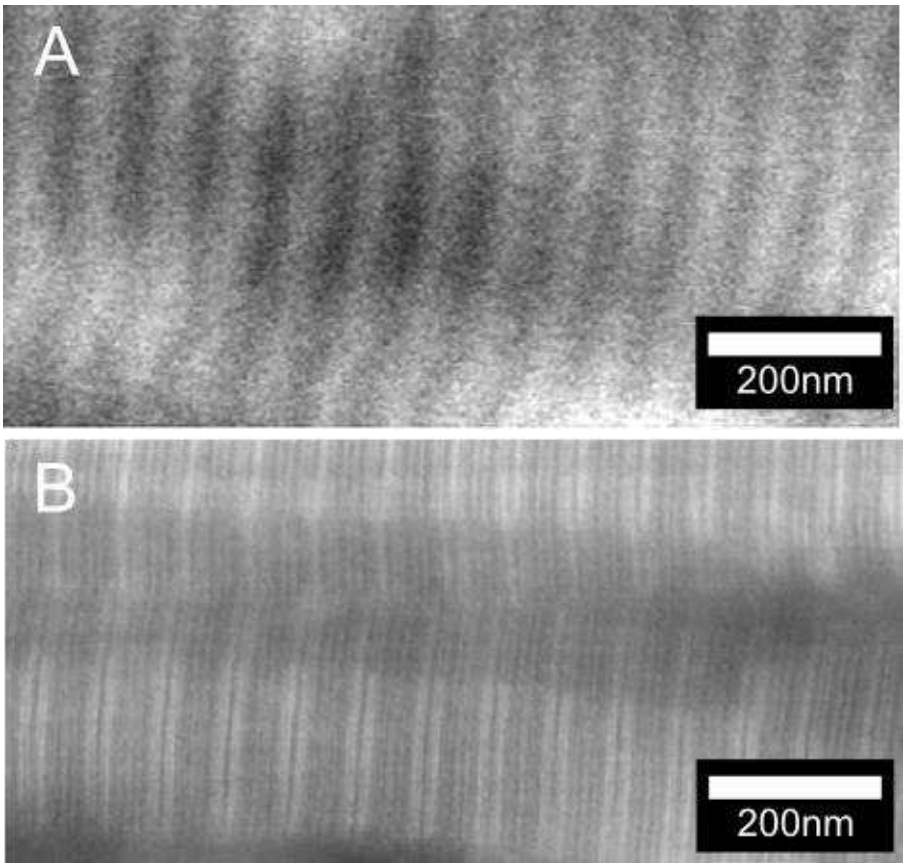

Figure 1 Representative ADF-STEM images of unstained (A) and stained (B) collagen fibrils in oim tail tendon. Brighter regions in (A) are regions with overlapping collagen molecules, while in darker regions there are gaps between the molecules. Brighter regions in (B) correspond to charged regions, which attract the staining agent. Images were taken on Titan at Imperial College.

Investigation of the transverse section of mouse tail tendon showed regions composed of approximately circular fibril cross-section (Figure SI2). The assessment of the cross-sectional area revealed that the average fibril cross-sections had significantly larger areas in WT than in oim specimens (WT=48±29 nm^2 vs. oim=34±20 nm^2) and the oim fibrils rarely reached the sizes observed in WT tissues (1st quartile-3rd quartile: WT=20-71 nm^2 vs. oim=17-49 nm^2).

In oim collagen, abnormal, fibrillar structures, as well as mature, fully developed fibrils similar to WT (Figure 2A, B), were present. The abnormal fibrils in oim were loosely packed and many of them were significantly kinked (Figure 2C, white arrowhead). Regions with formation of many circular and poorly packed assemblies of fibrils were also observed (Figure 2C, black arrowhead). In WT tissue, the circular assemblies or significant kinking of the fibrils were not observed.

At the nanometre scale in both WT and oim, sub-fibrillar regions were observed (Figure 2D, E, F). These disorganized regions appeared to consist of finer sub-fibrils of 10 nm in diameter. Bundles of sub-fibrils still displayed a faint banding pattern (Figure 2E, black arrowheads). In oim, large regions formed of sub-fibrils were observed. Regions containing sub-fibrils in WT were relatively small and distributed among fully developed fibrils tissues (Figure 2A, D). Interestingly, some of the sub-fibrils also show their own banding (Figure 2F).

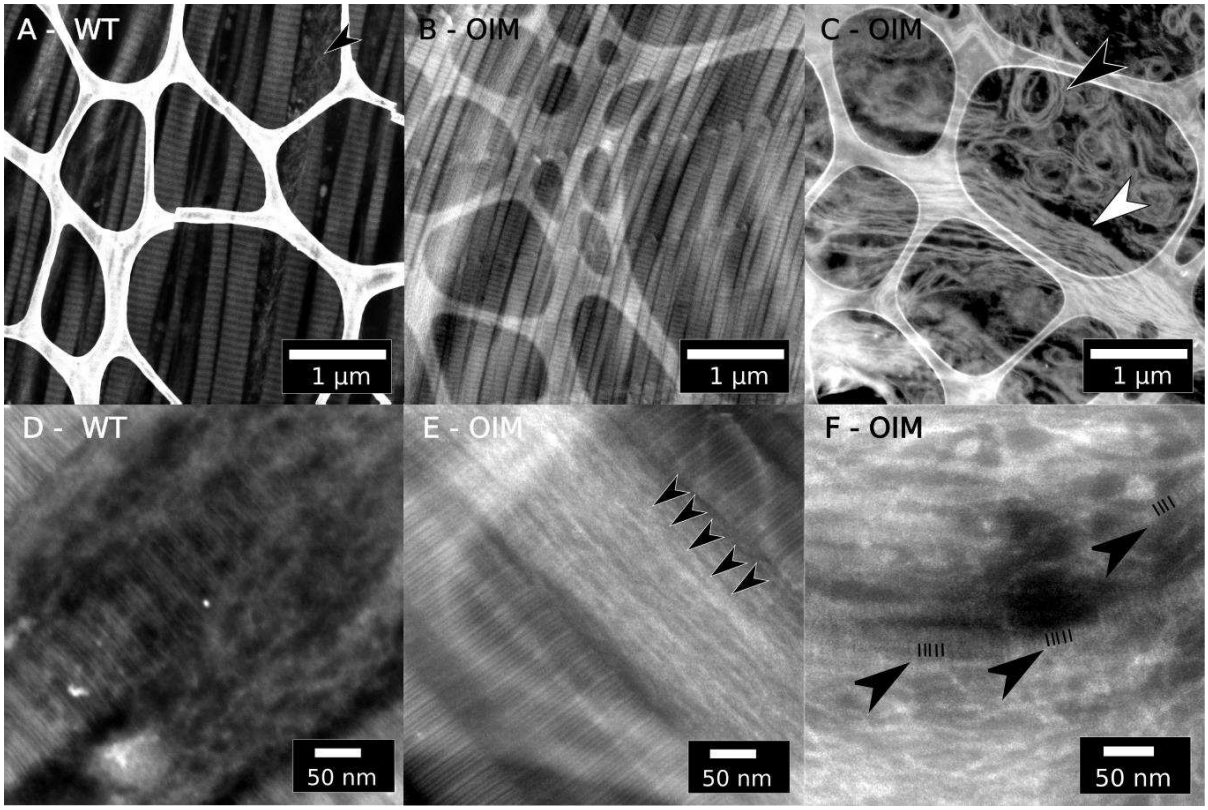

Figure 2 Representative ADF-STEM images of osmium tetroxide-stained collagen fibrils from tail tendon of WT (A, D) and oim (B, C, E, F) and mice observed on a Titan microscope at 300kV. Sections were placed on grids with a lacey carbon support, which is visible in images A, B, C and E. (A) Longitudinal sections of WT collagen fibrils. Regions containing mature fibrils coexist with regions composed of sub-fibrils (black arrowhead). (B) Longitudinal sections of fully developed oim collagen fibrils. (C) Longitudinal, irregularly oriented, poorly packed collagen fibrils of oim mice at the micrometre scale. Fibrils are grouped into loose bundles and may bend (white arrow head). Fibrils of OIM mouse tail tendon may also form poorly packed circular assemblies (black arrowhead). (D) Poorly packed bundles of fine, disordered collagen matrix observed in the wild type. (E) At nano-scale, a faint banding pattern can be observed (black arrowheads point the darker bands) in regions with sub-fibrils observed in oim. (F) Some sub-fibrils may exhibit a sub-banding pattern (black arrowheads, black lines highlight the faint sub-banding). Images were taken on Titan at Imperial College.

3.2. Organization of mineral in collagen matrix of WT and oim mice

At higher magnifications, crystals observed in bone of WT and oim mice displayed features typical for mineralized collagen. Mineral platelets were usually observed edge-on giving the appearance of needle-like crystals. Crystals were aligned with the long axis of collagen fibrils (Figure 3A). In oim, this alignment was less apparent (Figure 3C).

SAED diffraction patterns confirmed mineralized regions, in both WT and oim bone, were indexed as crystalline hydroxyapatite (HA) (Figure 3). SAED diffraction patterns collected from various regions without distinctive banding pattern of WT and oim tissue exhibited very similar texturing in organized and disorganized regions (Figure SI3). In disorganized regions, (002) reflections form full rings, sometimes segmented into few disconnected arcs. However, a small degree of order might be still maintained as the (002) ring showed an increase in the intensity in one direction. The orientation of crystals in WT and oim tissue was assessed by measuring the angles of arcs of the (002) plane reflections of the SAED patterns (Figure 4). The mean arc angle was similar in WT and oim tissues (WT=44.2±8.7° vs. oim=45.1±9°); however, the spread of data over two times larger in oim than in WT (1st quartile-3rd quartile: ΔWT=6.8° vs. Δoim=17.0°).

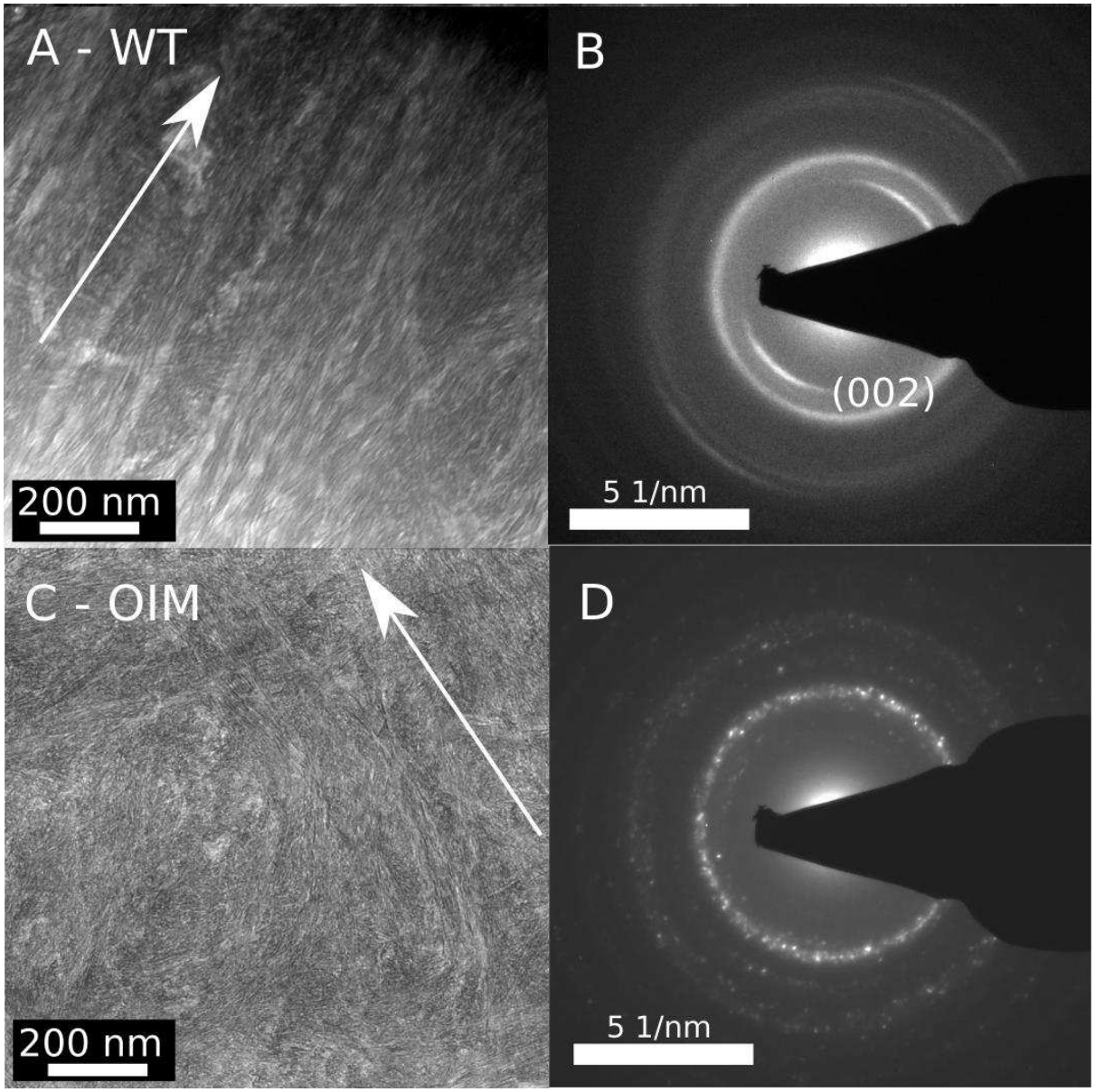

Figure 3 Representative BF-TEM images of WT (A, B) and oim (C, D) bone regions with corresponding indexed SAED patterns observed on the Titan TEM. The approximate alignment of collagen fibrils is indicated by white arrows. Fibrils in oim bone appear more tortuous and tend to branch and change direction than in the control WT tissue. The WT bone exhibited (002) arcs aligned with fibrils (B), while in oim bone (002) arcs were often absent in region of less organized fibrils (D). Images were taken on Titan at Imperial College.

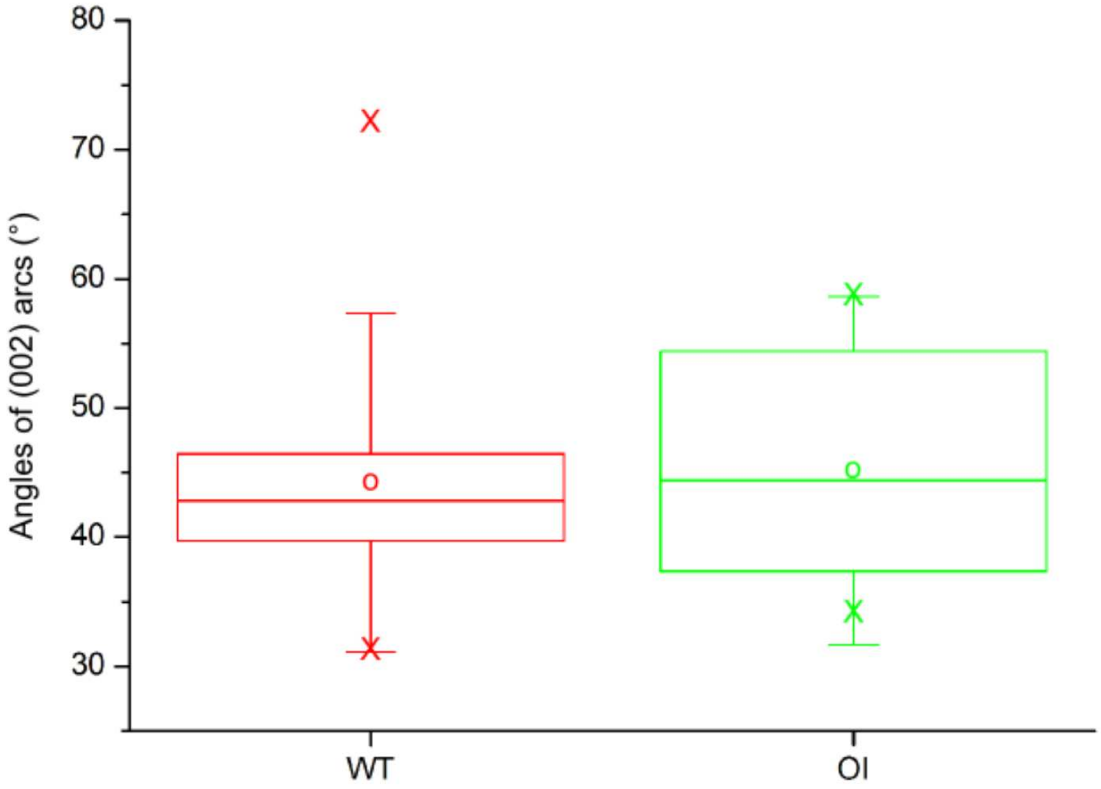

Figure 4 Conventional box plots were used to show changes in the length of the (002) arcs between wild type (WT) and oim (OI) bone specimens (n=30 regions for each group). WT and oim arcs have a similar mean length, but the distribution of oim arc lengths is much wider.

3.3. EELS analysis of the chemical composition of the collagen and mineral in WT and oim bone

EELS can be used to probe the chemical composition and bonding environment of atoms in the examined material. Electrons travelling through a sample can lose energy due to the excitation of inner-shell electrons to unoccupied states above the Fermi-level. These energy-losses (known as core-losses) occur at characteristic onset energies that can be related to the presence of specific elements. In the present study, the K-edges of carbon (onset at ~283eV), nitrogen (~396eV) and oxygen (~530eV), and the $L_{2,3}$-edges of phosphorus (~134eV) and calcium (~344eV) were examined. K-edges arise due to excitation of 1s electrons, and $L_{2,3}$-edges arise due to excitation of 2p electrons. The shape of the spectrum after the initial onset, referred to as the energy-loss near-edge structure (ELNES), can provide insight into the

bonding environment within a compound. EELS was not performed on the tail tendon samples as the stain alters the bonding environment and the observed ELNES.

For EELS analysis, transverse sections of WT and oim bone were selected (Figure SI4). Circular regions of high intensity were initially classified as more mineralised and their surrounding was classified as less mineralised. Regions labelled as more mineralised showed more intense signals at the Ca-K and P-$L_{2,3}$ edges. Regions labelled as less mineralised showed less intense signals at the Ca-K and P-$L_{2,3}$ edges. Approximate regions of mineralised WT bone could be identified readily in the micrographs (Figure SI4 A). In comparison, oim sections showed a smaller variation in contrast and it was more difficult to distinguish between more and less mineralised regions (Figure SI4 B).

3.3.1. Phosphorus $L_{2,3}$-edge

The ELNES of the phosphorus $L_{2,3}$-edge exhibits three main peaks: A, B and C at ~138, ~141 and ~147eV, respectively. These features were followed by a broad feature D with maximum at ~160eV (Figure SI5 I). Phosphorus spectra were normalized and aligned to the first peak A, which was set to an energy-loss of 138 eV based on published data.[36]

Peaks A and C are associated with transitions from core 2p to a p-like (A) and a d-like (C) states, respectively.[36] Peak B was observed in calcium-containing minerals.[36] Peak D was attributed to a cross-section maximum of 2p state transitions and multiple scattering.[37]

In mineralized tissues, the phosphorus $L_{2,3}$-edge features did not vary between WT and oim model (Figure SI5 I).

3.3.2. Calcium $L_{2,3}$-edge

In mineralized bone, the calcium $L_{2,3}$-edge spectra exhibited characteristic, so-called white line peaks A and B at ~348 and ~351 eV, respectively (Figure SI5 II). The calcium spectra were aligned and normalized to the peak A, which was set to 348 eV based on literature.[38]

The calcium $L_{2,3}$ edge spectra of oim and WT bone did not exhibit significant differences (Figure SI5 II).

3.3.3. Oxygen K-edge

The typical spectrum of mineralized bone of WT and oim mice (Figure SI5 III) shows a double peak B-C at ~537 and ~539eV, respectively, and a weak peak D at ~545eV. In a few

spectra, a small peak A at ~532eV was observed (OIMintra, WTintra, Figure SI5 III). Oxygen spectra of mineralized regions were aligned using peak C set to 539eV. Spectra were normalized to the most intense peak of each individual spectrum.

Feature A may be attributed to C=O transitions in carboxyl or amide groups in amino acids in protein[39,40] or C=O transitions in carbonated mineral.[26] Peaks B, C and D originate solely from transitions in the mineral phase. Peaks B and C were assigned to combined transitions of electrons in oxygen atoms to p-like states.[26] Peak D was assigned to transitions to 4s- and 4p-like states in oxygen bonds.

Typically, the intrinsic variability of biological material makes interpretation of oxygen K-edge challenging. Indeed, the oxygen K-edges structures consisted of a mixture of features characteristic of collagen and apatite and did not show significant variation between mineralized WT and *oim* tissue (Figure SI5 III).

3.3.4. Carbon K-edge

In the majority of spectra collected from WT and oim bone, peak A at ~285eV was absent or present only in the form of a more intense shoulder on peak B (Figure 5). Spectra of oim and WT bone usually started with peak B at ~286eV. Peak B was followed by small peaks C at ~287eV, C* at ~288eV and D* at ~289eV, and a pronounced peak D at ~290eV. Peak D was found more frequently in oim bone. Spectra of mineralized tissue were normalized to peak B and calibrated to peak D set to standard 290eV based on the literature.[41]

Characteristic energies corresponding to different types of molecular bonds were compiled mostly from X-ray absorption near edge structure (XANES) studies and presented in Table 1. Peak A was assigned to 1s-π* C-C transitions.[42] Peak B was assigned to transitions in aromatic carbon or carbonyl groups.[43–45,39] Peak C can be attributed to 1s-σ* C-H transitions in an aliphatic[40] or a diamond-like bond[46], 1s-π* C=O transitions in peptide bonds in carbonyl[43,46] or amidyl[40] and 1s-π* C=O transitions in carboxyl[40]. Electron transitions resulting in the formation of peak C* might be connected to C≡N, C=O, C=C or C-H excitations in nitrile, enol, aliphatic or aromatic groups.[39,40,43,47] Peak D* might originate from transitions in various carbon-oxygen and carbon-nitrogen groups in nucleic acids.[40,47,48] Peak D was characteristic of carbonate 1s-π*-A transitions.[41]

Table 1 Approximate transitions in 285-294eV range in carbon K-edge fine structure and assignments of peaks.

Peak	Bonds and proposed assignments	Energy-loss (eV)
A	Double-bonded carbon C=C, amorphous carbon, graphite , protonated or alkylated aromatic carbon, peptide nucleic acid	284.9-285.5 [39,42,44,45,49,50]
B	Aromatic carbonyl C=O, aromatic C-OH	285.8-286.5 [39,40,43–45,51]
B, C	Nitrile C≡N	286.7-286.9 [40]
C	Aromatic C-OH, aliphatic C=O, enol C-OR	287.1-287.4 [39,40,44,45,52–54]
C*	Aromatic carbonyl C=O, amidyl	287.7-288.3 [39,40,44,45,51]
C*	CH_3, CH_2, CH	287.0-288.5 [39,40,44,45,55,56]
C*, D*	Carboxyl COOH, COO, carboxyamide, C=N, C-N	288.0-288.7 [39,40,43–45,53,57]
D*	C-OH, alcohol, polysaccharide	289.3-289.5 [39,40,44,45,53,54]
D	Carbonate	290.0-290.2 [40–42]

The most noteworthy difference between various regions of wild type (WT) and oim spectra was in the presence and intensity of peak D, which is characteristic of transitions of carbonate groups. [35–37] The carbonate peaks in oim bone often appeared as much more intense than in WT (Figure 5). Furthermore, in oim bone spectra showing the most intense peak D (Figure 5, OIM2, OIM3, OIM4), the shoulder E (~294eV) of a broad, high-energy peak was observed,

which might be assigned to carbonate 1s→σ*-C and π*-C transitions.[58] Additionally in oim spectra, peaks in the energy range 286-290 eV were less intense and closer to the background noise level; this is particularly obvious when observed with finely monochromated EELS, Figure SI6, where the peaks, when present, are very well resolved and separated. These peaks are mostly related to functional groups associated with organic compounds, which suggests adecrease in the collagen to mineral ratio.

We also observed a large inhomogeneity in the distribution of carbonate within tissues (Figure 5). We examined 50 different regions of both, WT and oim. There were regions with no carbonate detected (WT= 45% vs. oim=39%), regions where the carbonate signal was localized in <100 nm "spots" (WT= 17% vs. oim=25%) and regions with a seemingly homogeneous distribution of carbonate (WT= 38% vs. oim=36%).

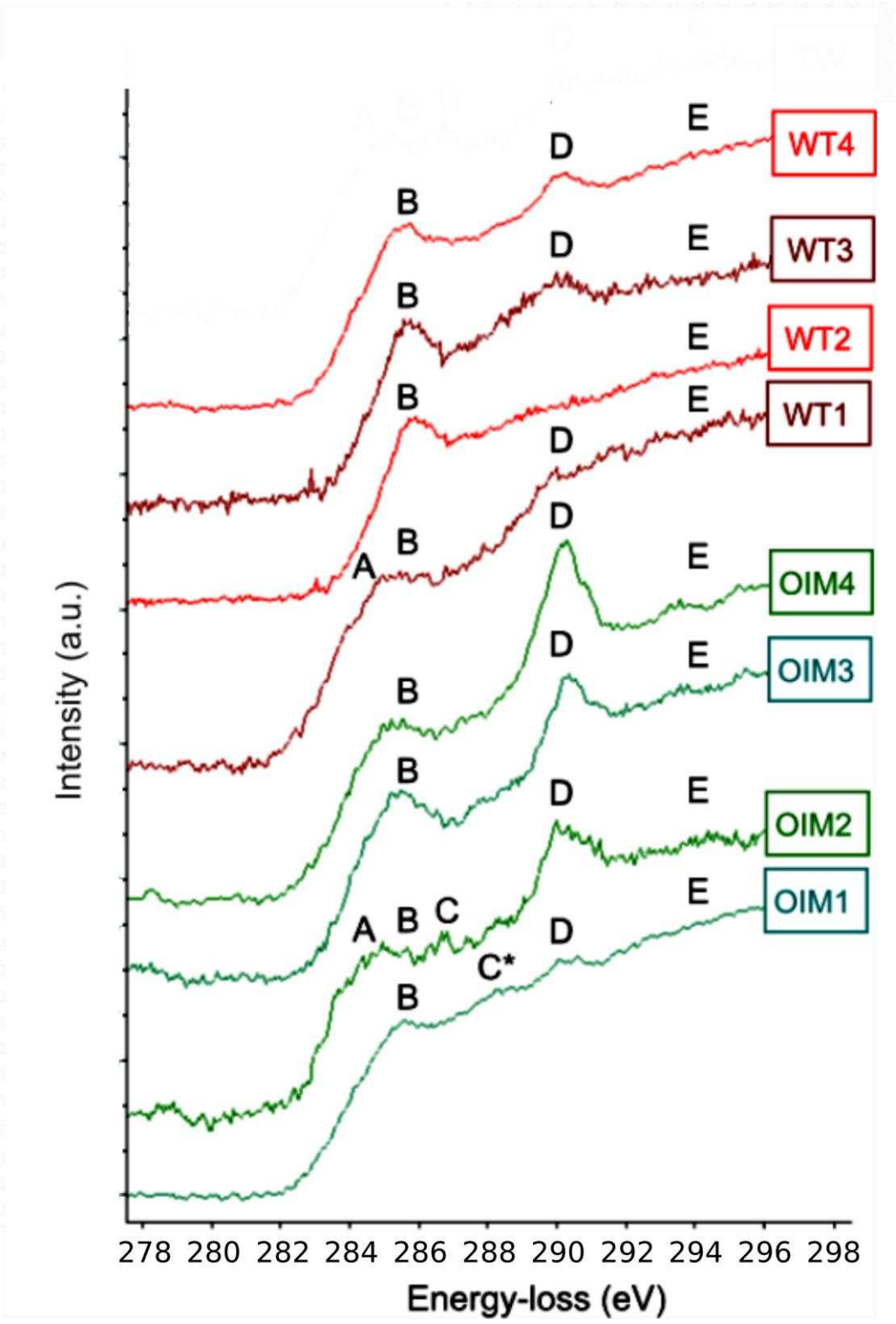

Figure 5 The carbon K near edge structures of mineralized bone of wild type (WT) and oim mice (OIM). The carbonate peak D at ~290eV observed in oim species is usually more intense than in WT. Formation of fine peaks on the shoulder E (~294eV) of a broad, high-energy peak was observed in OIM2-4, which might be assigned to carbonate 1s→σ*-C and π*-C transitions. Spectra WT1-3 and OIM1-3 were collected on Titan at Imperial College. Spectra WT4 and OIM4 were collected at SuperSTEM.

3.3.5. Nitrogen K-edge

The nitrogen K-edge spectra of mineralized oim and WT bone (Figure 6) exhibits two peaks A and B at ~400 and ~401 eV, respectively, followed by a broad peak C at ~408 eV. Nitrogen spectra in mineralized tissue were aligned to the peak A of calcium edge set to 348 eV based on published literature[38] and normalized to the most intense peak (A or B). The calibration of energy scale was confirmed by observation of the zero loss peak before and after the acquisition.

Peak A might be associated with 1s-π* transitions from nitrogen in an aromatic ring[39,59–61], which is an essential part of collagen crosslinking. Peak B might connected with 1s-π* transitions in the nitrated carbon structure, most likely in glycine, [61,62] oxidized pyridine [39,59] or 1s-π* transitions in amide groups (C=ONH)[48]. The broad peak C is attributed more generally to 1s-σ* transitions in amino compounds,[39] probably mostly originating from glycine.[48]

A variation in the relative intensity of peaks A and B is observed in neighbouring regions of bone (Figure 6). Monochromated STEM-EELS was employed to resolve the origins of variation seen in the intensity of peaks A and B, which were suspected to originate from the presence of non-glycine amino acids of collagen or changes in the oxidation of states of nitrogen. Changes observed in nitrogen K-edge may reflect the transformation of hydroxyimine- to pyridine-based crosslinks, which are connected to maturation of the collagen matrix, [63] and the capability to nucleate and proliferate the mineral [10,63–67]

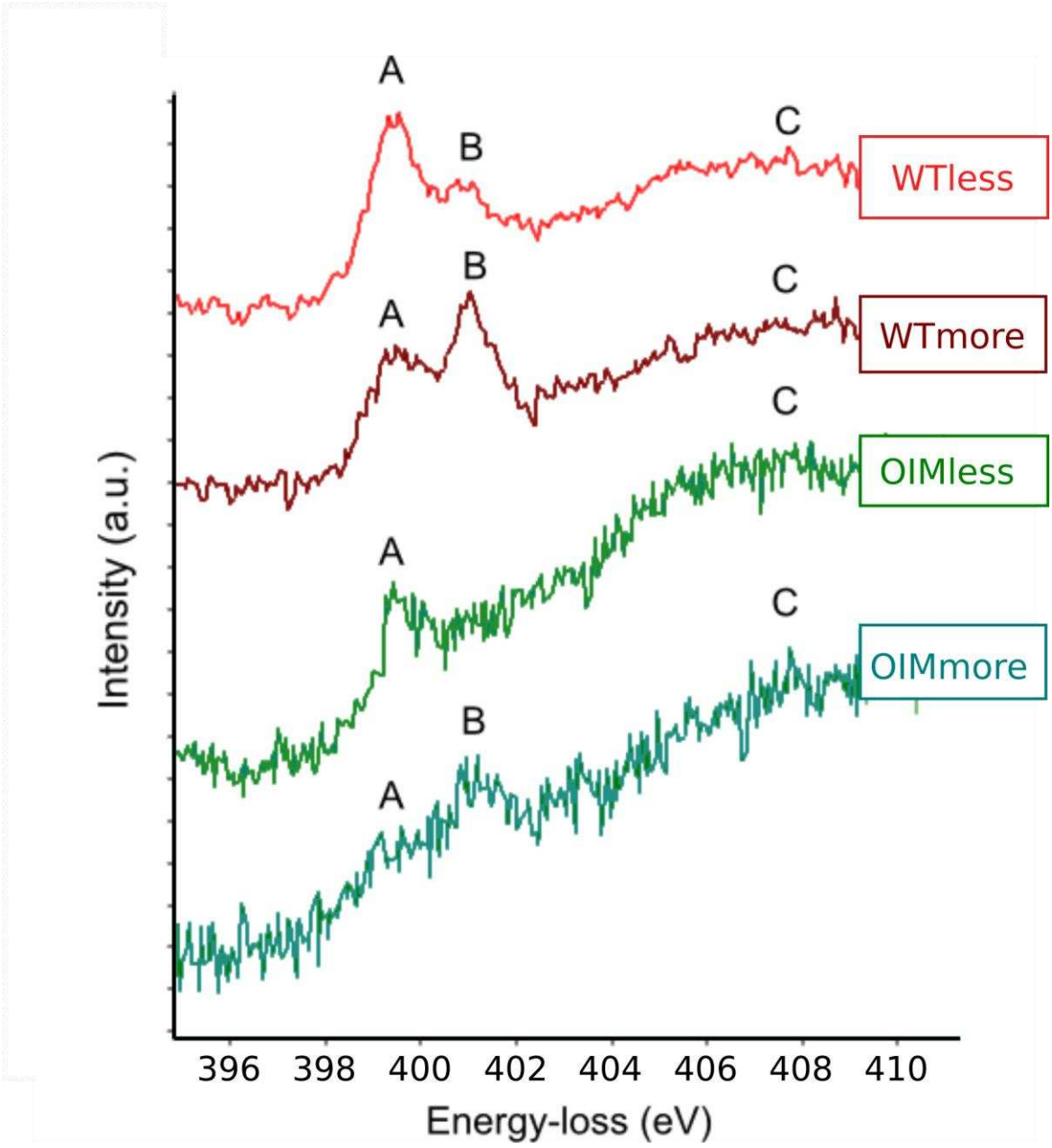

Figure 6 The nitrogen K near edge structures of more and less mineralized regions of bone of wild type (WTmore/less) and oim (OIMmore/less) mice taken from transverse sections of the tissue. Presented spectra were collected on Titan at Ohio State University.

4. Discussion & conclusions

Marked alterations in the substructure and organisation of the collagen fibrils in oim tail tendon were shown, including kinking and lack of banding. Although these alterations are expected in oim from bulk analyses, which take average measurements,[7,15,18] we were able to

show, using high resolution TEM, that some regions of the oim tissues were still able to form collagen fibrils with the characteristic periodic banding pattern of collagen type I fibrils, identical to that in WT bone and tendon. The mature oim collagen fibrils, however, had smaller diameters than fibrils seen in WT tendon and crystals within oim fibrils were less organized. Interestingly, for both cases the difference was in the variation/dispersion of values, while the mean values were similar between WT an oim. These findings are consistent with studies showing similar mean values of the periodic banding in WT and oim, but with the oim bone having a wider distribution of values.[68]

Regions of disorganized fibrils were observed in the WT and oim bone and tendon. Disorganized regions in oim tissues were observed to cover extended areas, over few micrometres in length, in contrast disorganized regions in the WT tissues were only few hundred nanometres in length.

At the micrometre scale, the malformations resembled a loosely packed, collagen structure similar to those observed in woven bone. Malformed structures consisted of randomly distributed thin, collagen fibrils, often bent or twisted, devoid of the banding pattern. Similar micro-defects of collagen fibrils were previously observed only in human OI tendon and bone tissues.[69,70]

At the nanometre scale, the sub-fibrillar collagen assemblies, which exhibited no or a very faint banding pattern, were observed. These disorganized structures resemble structures observed in untwisted collagen fibrils in cornea[71] and might be identical microribbons seen at early stages of fibrillogenesis.[72] If the observed sub-fibrils represent early stages of fibrillogenesis, their significant presence in oim tissues could be a result of a more intense turnover of the collagen matrix[2] and/or accumulation of sub- fibrils with time.[73] It is not clear, however, what factors might hinder the formation of mature fibrils in oim.

Modelling studies of collagen molecules in oim have suggested that malformation of collagen triple helices result in kinked molecules, which limit or even prevent formation of a mature fibril.[8,74] However, previous in vitro TEM studies of oim fibrils in tendon have reported only the formation of straight, banded collagen.[7,9] In this work, we have shown that straight and malformed fibrils coexist in oim tissue. This finding suggests that the fibril assembly in oim might be hindered by other factors (i.e. by the presence of non-collagenous proteins) rather than the altered collagen structure alone.

Chemical analysis did not show modifications between WT and oim tissues in the chemistry of mineral phase. However, we observed variations in carbon and nitrogen species within all examined tissues. Observed variations only occasionally followed the initial division into the more and less mineralised regions, and often appeared disconnected from any structural features observed in the tissue. This might be caused by the natural variation in the tissue or could be caused by the oblique orientation of examined sections. While the spatial distribution of chemical changes requires further studies, we can discuss the possible origins of chemical variations within bone tissue.

Our observations suggest that mineral nucleating in WT and oim bone possesses the major structural and chemical characteristics of carbonated apatite. We did not observe any significant variations in the carbonate content between WT and oim. However, spatially resolved EELS of carbon K-edge revealed marked local changes in the amount of carbonate ions found within different regions of both WT and oim bone. Some studies suggested that spatial variations of carbonate content of the mineral may play an important role in altering the mechanical integrity of the bone at larger length scales.[75] Our EELS data is not consistent with recent FTIR measurements on oim bone. In contrast to EELS, FTIR has shown that the carbonate-to-phosphate ratio of the mineral is lower in OI bone.[22,23] This difference between measured values may be attributed to the fact that FTIR only assigns the B-type CO_3^{2-} substitution in carbonated HA or may be related to spatial variations in the chemistry of bone, which are averaged out with FTIR. The variance in carbonate/phosphate ratio acquired from spectroscopic techniques may also arise from the polarization of the beam and the orientation of the specimen.[76,77] Future work will conduct correlative studies between EELS and Raman to resolve this apparent inconsistency.

Most of the mechanical properties of bone depend on the nanostructure of collagen molecules and their interactions with mineral. Formation of crosslinks is not only important for defining the fibril stability and mechanical properties, but may also be beneficial for the mineralisation process.[78] However there is no single technique available to prove these relationships between structure, chemistry and the properties of the collagen and mineral. In this work, the capability of monochromated STEM-EELS in mapping functional groups on mineralized collagen has been very clearly demonstrated for a disease in which genetic alterations result in molecular deficits of collagen. Monochromated EELS spectra collected from various regions of bone at the nitrogen K-edge exhibited distinct changes in fine structure and

intensity. Observed variations were tenatively related to the presence of non-glycine amino acids or modification of nitrogen oxidation states [39,59], which may be connected to the maturation of collagen nucleation sites or crosslinks.[10,63–65] Particularly, transformation of bivalent hydroxyimine crosslinks into trivalent pyridine-based ones and associated changes in the oxidation states of nitrogen-containing groups might be related to the formation of nucleation sites in collagen. [63,79,80] In turn, the spatial distribution of these signatures might describe the evolution mineral within collagen.

These studies advocate the need for further investigations on the chemical variation in collagen and mineral at the nano-scale as they may reflect mineralisation process in two ways: directly highlighting the nucleation sites and indirectly showing collagen matrix modifications. Ongoing studies in our group using knock-out models with altered cross linking and other deficiencies in other non-collagenous proteins will be used to further test these hypotheses. We suggest that these analytical results open the door for compelling new sets of EELS experiments that can provide detailed information about the distribution and chemical nature of functional groups on the collagen and their role in collagen formation and mineralisation. Here we have identified nano-structural changes in oim tissue that has not been identified with bulk techniques. This not only provides an understanding of how molecular changes in the collagen in OI leads to brittle bones, but also gives insight into the necessary composition and structural features, which template collagen mineralization.

Acknowledgements

This research was funded by the UK Engineering and Physical Sciences Research Council. MMK acknowledges support from Armourers & Brasiers' Gauntlet Trust. DWM acknowledges support from the Ohio Third Frontier program though the Ohio Research Scholar award. AEP acknowledges an ERC individual starting investigator grant (CNTBBB) and an Elsie Widdowson research fellowship from Imperial College London. Part of the STEM-EELS data was collected at the SuperSTEM Laboratory, the U.K National Facility for Aberration-Corrected STEM, supported by the Engineering and Physical Sciences Research Council (EPSRC).

Supporting information

Figures S1-S5

Table SI1

Bibliography

(1) Martin, E.; Shapiro, J. R. Osteogenesis imperfecta: epidemiology and pathophysiology. Curr. Osteoporos. Rep. **2007**, 5 (3), 91–97.

(2) Forlino, A.; Cabral, W. A.; Barnes, A. M.; Marini, J. C. New perspectives on osteogenesis imperfecta. Nat. Rev. Endocrinol. **2011**, 7 (9), 540–557.

(3) Chipman, S. D.; Sweet, H. O.; McBride, D. J.; Davisson, M. T.; Marks, S. C.; Shuldiner, A. R.; Wenstrup, R. J.; Rowe, D. W.; Shapiro, J. R. Defective pro alpha 2 (I) collagen synthesis in a recessive mutation in mice: a model of human osteogenesis imperfecta. Proc. Natl. Acad. Sci. U. S. A. **1993**, 90 (5), 1701.

(4) Kuznetsova, N.; McBride Jr, D.; Leikin, S. Osteogenesis Imperfecta Murine: Interaction Between Type I Collagen Homotrimers. J. Mol. Biol. **2001**, 309 (3), 807–815 DOI: 10.1006/jmbi.2001.4682.

(5) Kuznetsova, N. V.; McBride Jr., D. J.; Leikin, S. Changes in Thermal Stability and Microunfolding Pattern of Collagen Helix Resulting from the Loss of a2(I) Chain in Osteogenesis Imperfecta Murine. J. Mol. Biol. **2003**, 331, 191–200.

(6) Landis, W. J. The strength of a calcified tissue depends in part on the molecular structure and organization of its constituent mineral crystals in their organic matrix. Bone **1995**, 16 (5), 533–544.

(7) McBride, D. J.; Choe, V.; Shapiro, J. R.; Brodsky, B. Altered collagen structure in mouse tail tendon lacking the [alpha] 2 (I) chain1. J. Mol. Biol. **1997**, 270 (2), 275–284.

(8) Chang, S.-W.; Shefelbine, S. J.; Buehler, M. J. Structural and Mechanical Differences between Collagen Homo- and Heterotrimers: Relevance for the Molecular Origin of Brittle Bone Disease. Biophys. J. **2012**, 102 (3), 640–648 DOI: 10.1016/j.bpj.2011.11.3999.

(9) Miles, C. The Role of the α2 Chain in the Stabilization of the Collagen Type I Heterotrimer: A Study of the Type I Homotrimer in oim Mouse Tissues. J. Mol. Biol. **2002**, 321 (5), 797–805 DOI: 10.1016/S0022-2836(02)00703-9.

(10) Kirsch, E.; Krieg, T.; Remberger, K.; Fendel, H.; Bruckner, P.; Muller, P. K. Disorder of collagen metabolism in a patient with osteogenesis imperfecta (lethal type): increased degree of hydroxylation of lysine in collagen types I and III. Eur. J. Clin. Invest. **1981**, 11 (1), 39–47.

(11) Tenni, R.; Cetta, G.; Dyne, K.; Rossi, A.; Quacci, D.; Lenzi, L.; Castellani, A. A. Type I procollagen in the severe non-lethal form of osteogenesis imperfecta. Hum. Genet. **1988**, 79 (3), 245–250.

(12) Sims, T. J.; Miles, C. A.; Bailey, A. J.; Camacho, N. P. Properties of Collagen in OIM Mouse Tissues. Connect. Tissue Res. **2003**, 44 (1), 202–205 DOI: 10.1080/03008200390181663.

(13) Carriero, A.; Zimmermann, E. A.; Paluszny, A.; Tang, S. Y.; Bale, H.; Busse, B.; Alliston, T.; Kazakia, G.; Ritchie, R. O.; Shefelbine, S. J. How tough is Brittle Bone? Investigating Osteogenesis Imperfecta in Mouse Bone. J. Bone Miner. Res. **2014**.

(14) Vetter, U.; Fisher, L. W.; Mintz, K. P.; Kopp, J. B.; Tuross, N.; Termine, J. D.; Gehron-Robey, P. Osteogenesis imperfecta: Changes in noncollagenous proteins in bone. J. Bone Miner. Res. **1991**, 6 (5), 501–505.

(15) Fratzl, P.; Paris, O.; Landis, W. J.; Klaushofer, K. Mineral crystals are smaller and less oriented in osteogenesis imperfecta mouse model, as revealed by small-angle X-ray scattering. In Bone; 1995; Vol. 16, p 407.

(16) Vanleene, M.; Porter, A.; Guillot, P.-V.; Boyde, A.; Oyen, M.; Shefelbine, S. Ultra-structural defects cause low bone matrix stiffness despite high mineralization in osteogenesis imperfecta mice. Bone **2012**, 50 (6), 1317–1323 DOI: 10.1016/j.bone.2012.03.007.

(17) Vetter, U.; Eanes, E. D.; Kopp, J. B.; Termine, J. D.; Robey, P. G. Changes in apatite crystal size in bones of patients with osteogenesis imperfecta. Calcif. Tissue Int. **1991**, 49 (4), 248–250.

(18) Fratzl, P.; Paris, O.; Klaushofer, K.; Landis, W. J. Bone mineralization in an osteogenesis imperfecta mouse model studied by small-angle x-ray scattering. J. Clin. Invest. **1996**, 97 (2), 396.

(19) Grabner, B.; Landis, W. J.; Roschger, P.; Rinnerthaler, S.; Peterlik, H.; Klaushofer, K.; Fratzl, P. Age-and genotype-dependence of bone material properties in the osteogenesis imperfecta murine model (oim). Bone **2001**, 29 (5), 453–457.

(20) Landis, W. J. Mineral characterization in calcifying tissues: atomic, molecular and macromolecular perspectives. Connect. Tissue Res. **1996**, 34 (4), 239–246.

(21) Dubey, D. K.; Tomar, V. Effect of osteogenesis imperfecta mutations in tropocollagen molecule on strength of biomimetic tropocollagen-hydroxyapatite nanocomposites. Appl. Phys. Lett. **2010**, 96 (2), 23703 DOI: 10.1063/1.3279158.

(22) Camacho, N. P.; Hou, L.; Toledano, T. R.; Ilg, W. A.; Brayton, C. F.; Raggio, C. L.; Root, L.; Boskey, A. L. The material basis for reduced mechanical properties in oim mice bones. J. Bone Miner. Res. **1999**, 14 (2), 264–272.

(23) Vanleene, M.; Saldanha, Z.; Cloyd, K. L.; Jell, G.; Bou-Gharios, G.; Bassett, J. H. D.; Williams, G. R.; Fisk, N. M.; Oyen, M. L.; Stevens, M. M.; et al. Transplantation of human fetal blood stem cells in the osteogenesis imperfecta mouse leads to improvement in multiscale tissue properties. Blood **2011**, 117 (3), 1053–1060 DOI: 10.1182/blood-2010-05-287565.

(24) Kozloff, K. M.; Carden, A.; Bergwitz, C.; Forlino, A.; Uveges, T. E.; Morris, M. D.; Marini, J. C.; Goldstein, S. A. Brittle IV Mouse Model for Osteogenesis Imperfecta IV Demonstrates Postpubertal Adaptations to Improve Whole Bone Strength. J. Bone Miner. Res. **2004**, 19 (4), 614–622 DOI: 10.1359/JBMR.040111.

(25) Bala, Y.; Farlay, D.; Boivin, G. Bone mineralization: from tissue to crystal in normal and pathological contexts. Osteoporos. Int. **2013**, 24 (8), 2153–2166 DOI: 10.1007/s00198-012-2228-y.

(26) Kłosowski, M. M.; Friederichs, R. J.; Nichol, R.; Antolin, N.; Carzaniga, R.; Windl, W.; Best, S. M.; Shefelbine, S. J.; McComb, D. W.; Porter, A. E. Probing carbonate in bone forming minerals on the nanometre scale. Acta Biomater. **2015**, 20, 129–139 DOI: 10.1016/j.actbio.2015.03.039.

(27) Kłosowski, M. M.; Shefelbine, S. J.; Porter, A. E.; McComb, D. W. Analytical Electron Microscopy of Bone and Mineralized Tissue. In Handbook of Imaging in Biological Mechanics; CRC Press, 2014; pp 491–506.

(28) Armstrong, S. R.; Jessop, J. L. P.; Winn, E.; Tay, F. R.; Pashley, D. H. Denaturation Temperatures of Dentin Matrices. I. Effect of Demineralization and Dehydration. J. Endod. **2006**, 32 (7), 638–641 DOI: 10.1016/j.joen.2005.10.062.

(29) Nudelman, F.; Pieterse, K.; George, A.; Bomans, P. H. H.; Friedrich, H.; Brylka, L. J.; Hilbers, P. A. J.; de With, G.; Sommerdijk, N. A. J. M. The role of collagen in bone apatite formation in the presence of hydroxyapatite nucleation inhibitors. Nat. Mater. **2010**, 9 (12), 1004–1009 DOI: 10.1038/nmat2875.

(30) Quan, B. D.; Sone, E. D. Cryo-TEM Analysis of Collagen Fibrillar Structure. In Methods in Enzymology; Elsevier, 2013; Vol. 532, pp 189–205.

(31) Egerton, R. F.; Li, P.; Malac, M. Radiation damage in the TEM and SEM. Micron **2004**, 35, 399–409.

(32) Srot, V.; Bussmann, B.; Salzberger, U.; Koch, C. T.; van Aken, P. A. Linking Microstructure and Nanochemistry in Human Dental Tissues. Microsc. Microanal. **2012**, 18 (3), 509–523 DOI: 10.1017/S1431927612000116.

(33) McGilvery, C. M.; Goode, A. E.; Shaffer, M. S. P.; McComb, D. W. Contamination of holey/lacey carbon films in STEM. Micron **2012**, 43 (2–3), 450–455 DOI: 10.1016/j.micron.2011.10.026.

(34) Bruns, R. R. Supramolecular structure of polymorphic collagen fibrils. J. Cell Biol. **1976**, 68 (3), 521–538.

(35) Chapman, J. A.; Tzaphlidou, M.; Meek, K. M.; Kadler, K. E. The collagen fibril - A model system for studying the staining and fixation of the protein. Electron Microsc. Rev. **1990**, 3 (1), 143–182.

(36) Kruse, J.; Leinweber, P.; Eckhardt, K.-U.; Godlinski, F.; Hu, Y.; Zuin, L. Phosphorus L2,3 -edge XANES: overview of reference compounds. J. Synchrotron Radiat. **2009**, 16 (2), 247–259 DOI: 10.1107/S0909049509000211.

(37) Sutherland, D. G. J.; Kasrai, M.; Bancroft, G. M.; Liu, Z. F.; Tan, K. H. Si L-and K-edge x-ray-absorption near-edge spectroscopy of gas-phase Si (CH3)x(OCH3) 4-x: Models for solid-state analogs. Phys. Rev. B **1993**, 48 (20), 14989.

(38) Fleet, M. E.; Liu, X. Calcium L2,3-edge XANES of carbonates, carbonate apatite, and oldhamite (CaS). Am. Mineral. **2009**, 94 (8–9), 1235–1241 DOI: 10.2138/am.2009.3228.

(39) Lehmann, J.; Solomon, D.; Brandes, J.; Fleckenstein, H.; Jacobsen, C.; Thieme, J. Synchrotron-based near-edge X-ray spectroscopy of natural organic matter in soils and sediments. Biophys.-Chem. Process. Involv. Nat. Nonliving Org. Matter Environ. Syst. **2009**, 729–781.

(40) Westphal, S. W.; Yabuta, H. Quantitative Organic and Light Element analysis of Comet 81P/Wild 2 particles using C-, N-, and O-μ-XANES.

(41) Metzler, R.; Abrecht, M.; Olabisi, R.; Ariosa, D.; Johnson, C.; Frazer, B.; Coppersmith, S.; Gilbert, P. Architecture of Columnar Nacre, and Implications for Its Formation Mechanism. Phys. Rev. Lett. **2007**, 98 (26) DOI: 10.1103/PhysRevLett.98.268102.

(42) Garvie, L. A. J.; Craven, A. J.; Brydson, R. Use of electron-energy loss near-edge fine structure in the study of minerals. Am. Mineral. **1994**, 79, 411–425.

(43) Boese, J.; Osanna, A.; Jacoben, C.; Kirz, J. Carbon edge XANES spectroscopy of amino acids and peptides. J. Spectrosc. Relat. Phenom. **1997**, 85, 9–15.

(44) Cody, G. D.; Ade, H.; Wirick, S.; Mitchell, G. D.; Davis, A. Determination of chemical-structural changes in vitrinite accompanying luminescence alteration using C-NEXAFS analysis. Org. Geochem. **1998**, 28 (7), 441–455.

(45) Braun, A.; Kubatova, A.; Wirick, S.; Mun, S. B. Radiation damage from EELS and NEXAFS in diesel soot and diesel soot extracts. J. Electron Spectrosc. Relat. Phenom. **2009**, 170 (1–3), 42–48 DOI: 10.1016/j.elspec.2007.08.002.

(46) Ray, S. C.; Tsai, H. M.; Chiou, J. W.; Bose, B.; Jan, J. C.; Kumar, K.; Pong, W. F.; Dasgupta, D.; Tsai, M.-H. X-ray absorption spectroscopy (XAS) study of dip deposited a-C:H(OH) thin films. J. Phys. Condens. Matter **2004**, 16 (32), 5713–5719 DOI: 10.1088/0953-8984/16/32/008.

(47) Benzerara, K.; Yoon, T. H.; Tyliszczak, T.; Constantz, B.; Spormann, A. M.; Brown, G. E. Scanning transmission X-ray microscopy study of microbial calcification. Geobiology **2004**, 2 (4), 249–259.

(48) Gordon, M. L.; Cooper, G.; Morin, C.; Araki, T.; Turci, C. C.; Kaznatcheev, K.; Hitchcock, A. P. Inner-Shell Excitation Spectroscopy of the Peptide Bond: Comparison of the C 1s, N 1s, and O 1s Spectra of Glycine, Glycyl-Glycine, and Glycyl-Glycyl-Glycine. J. Phys. Chem. A **2003**, 107 (32), 6144–6159 DOI: 10.1021/jp0344390.

(49) Hitchcock, A. P.; Fischer, P.; Gedanken, A.; Robin, M. B. Antibonding s* valence MOs in the inner shell and outer shell spectra of the fluorobenzenes. J Phys Chem **1987**, 91, 531–540.

(50) Robin, M. B.; Ishii, I.; McLaren, R.; Hitchcock, A. P. Fluorination e€ ffects on the inner shell spectra of unsaturated molecules. J. Electron Spectrosc. Relat. Phenom. **1988**, 47, 53–92.

(51) Hitchcock, A. P.; Urquhart, S. G.; Rightor, E. G. Inner-shell spectroscopy of benzaldehyde, terephthalaldehyde, ethylbenzoate, terephthaloyl chloride and phosgene: models for core excitation of poly (ethylene terephthalate). J. Phys. Chem. **1992**, 96 (22), 8736–8750.

(52) Francis, J. T.; Hitchcock, A. P. Inner-shell spectroscopy of p-benzoquinone, hydroquinone, and phenol: distinguishing quinoid and benzenoid structures. J. Phys. Chem. **1992**, 96 (16), 6598–6610.

(53) Ishii, I.; Hitchcook, A. P. The oscillator strengths for C1< i> s</i> and O1< i> s</i> excitation of some saturated and unsaturated organic alcohols, acids and esters. J. Electron Spectrosc. Relat. Phenom. **1988**, 46 (1), 55–84.

(54) Sham, T. K.; Yang, B. X.; Kirz, J.; Tse, J. S. K-edge near-edge x-ray-absorption fine structure of oxygen- and carbon-containing molecules in the gas. Phys. Rev. A **1989**, 40 (2), 652–668.

(55) Hitchcock, A. P. Carbon K-shell excitation of gaseous and condensed cyclic hydrocarbons: C3H6, C4H8, C5H8, C5H10, C6H10, C6H12, and C8H8. J. Chem. Phys. **1986**, 85 (9), 4849 DOI: 10.1063/1.451719.

(56) Hitchcock, A. P.; Ishii, I. Carbon K-shell excitation spectra of linear and branched alkanes. J. Electron Spectrosc. Relat. Phenom. **1987**, 42 (1), 11–26.

(57) Ishii, I.; Hitchcock, A. P. A quantitative experimental study of the core excited electronic states of formamide, formic acid, and formyl fluoride. J. Chem. Phys. **1987**, 87 (2), 830 DOI: 10.1063/1.453290.

(58) Metzler, R. A.; Kim, I. W.; Delak, K.; Evans, J. S.; Zhou, D.; Beniash, E.; Wilt, F.; Abrecht, M.; Chiou, J.-W.; Guo, J.; et al. Probing the Organic−Mineral Interface at the Molecular Level in Model Biominerals. Langmuir **2008**, 24 (6), 2680–2687 DOI: 10.1021/la7031237.

(59) Vairavamurthy, A.; Wang, S. Organic Nitrogen in Geomacromolecules: Insights on Speciation and Transformation with K-edge XANES Spectroscopy. Environ. Sci. Technol. **2002**, 36 (14), 3050–3056 DOI: 10.1021/es0155478.

(60) Matsui, T.; Yudasaka, M.; Kikuchi, R.; Ohki, Y.; Yoshimura, S. Two kinds of nitrogen atoms in nitrogen-substituted, highly crystalline graphite prepared by chemical vapor deposition. Appl. Phys. Lett. **1994**, 65 (17), 2145 DOI: 10.1063/1.112774.

(61) Leinweber, P.; Kruse, J.; Walley, F. L.; Gillespie, A.; Eckhardt, K.-U.; Blyth, R. I. R.; Regier, T. Nitrogen K-edge XANES – an overview of reference compounds used to identify `unknown' organic nitrogen in environmental samples. J. Synchrotron Radiat. **2007**, 14 (6), 500–511 DOI: 10.1107/S0909049507042513.

(62) Bhattacharyya, S.; Lübbe, M.; Bressler, P. R.; Zahn, D. R. T.; Richter, F. Structure of nitrogenated amorphous carbon films from NEXAFS. Diam. Relat. Mater. **2002**, 11 (1), 8–15.

(63) Knott, L.; Tarlton, J. F.; Bailey, A. J. Chemistry of collagen cross-linking: biochemical changes in collagen during the partial mineralization of turkey leg tendon. Biochem. J. **1997**, 322 (Pt 2), 535.

(64) Knott, L.; Bailey, A. J. Collagen cross-links in mineralizing tissues: a review of their chemistry, function, and clinical relevance. Bone **1998**, 22 (3), 181–187.

(65) Landis, W. J.; Silver, F. H.; Freeman, J. W. Collagen as a scaffold for biomimetic mineralization of vertebrate tissues. J. Mater. Chem. **2006**, 16 (16), 1495 DOI: 10.1039/b505706j.

(66) Wise, E. R.; Maltsev, S.; Davies, M. E.; Duer, M. J.; Jaeger, C.; Loveridge, N.; Murray, R. C.; Reid, D. G. The Organic−Mineral Interface in Bone Is Predominantly Polysaccharide. Chem. Mater. **2007**, 19, 5055–5057 DOI: 10.1021/cm702054c.

(67) Pasteris, J. D.; Wopenka, B.; Freeman, J. J.; Rogers, K.; Valsami-Jones, E.; van der Houwen, J. A. M.; Silva, M. J. Lack of OH in nanocrystalline apatite as a function of degree of atomic order: implications for bone and biomaterials. Biomaterials **2004**, 25 (2), 229–238 DOI: 10.1016/S0142-9612(03)00487-3.

(68) Wallace, J. M.; Orr, B. G.; Marini, J. C.; Holl, M. M. B. Nanoscale morphology of Type I collagen is altered in the Brtl mouse model of osteogenesis imperfecta. J. Struct. Biol. **2011**, 173 (1), 146–152.

(69) Vogel, B. E.; Doelz, R.; Kadler, K. E.; Hojima, Y.; Engel, J.; Prockop, D. J. A Substitution of Cysteine for Glycine 748 of the 01 Chain Produces a Kink at This Site in the Procollagen I Molecule and an Altered N-Proteinase Cleavage Site over 225 nm Away. J. Biol. Chem. **1988**, 263, 19249–55.

(70) Cassella, J. P.; Stamp, T. C. B.; Ali, S. Y. A morphological and ultrastructural study of bone in osteogenesis imperfecta. Calcif. Tissue Int. **1996**, 58 (3), 155–165.

(71) Yamamoto, S.; Hashizume, H.; Hitomi, J.; Shigeno, M.; Sawaguchi, S.; Abe, H.; Ushiki, T. The Subfibrillar Arrangement of Corneal and Scleral Collagen Fibrils as Revealed by Scanning Electron and Atomic Force Microscopy. Arch Histol Cytol **2000**, 63 (2), 127–135.

(72) Jiang, F.; Hörber, H.; Howard, J.; Müller, D. J. Assembly of collagen into microribbons: effects of pH and electrolytes. J. Struct. Biol. **2004**, 148 (3), 268–278 DOI: 10.1016/j.jsb.2004.07.001.

(73) Han, S.; Makareeva, E.; Kuznetsova, N. V.; DeRidder, A. M.; Sutter, M. B.; Losert, W.; Phillips, C. L.; Visse, R.; Nagase, H.; Leikin, S. Molecular Mechanism of Type I Collagen Homotrimer Resistance to Mammalian Collagenases. J. Biol. Chem. **2010**, 285 (29), 22276–22281 DOI: 10.1074/jbc.M110.102079.

(74) Gajko-Galicka, A. Mutations in type I collagen genes resulting in osteogenesis imperfecta in humans. ACTA Biochim. Pol.-Engl. Ed.- **2002**, 49 (2), 433–442.

(75) Gourion-Arsiquaud, S.; Burket, J. C.; Havill, L. M.; DiCarlo, E.; Doty, S. B.; Mendelsohn, R.; van der Meulen, M. C.; Boskey, A. L. Spatial Variation in Osteonal Bone Properties Relative to Tissue and Animal Age. J. Bone Miner. Res. **2009**, 24 (7), 1271–1281 DOI: 10.1359/jbmr.090201.

(76) Garvie, L. A. J.; Craven, A. J.; Brydson, R. Parallel electron energy-loss spectroscopy (PEELS) study of B in minerals; the electron energy-loss near-edge structure (ELNES) of the B K edge. Am. Mineral. **1995**, 80 (11–12), 1132–1144 DOI: 10.2138/am-1995-11-1204.

(77) Aubaud, C.; Withers, A. C.; Hirschmann, M. M.; Guan, Y.; Leshin, L. A.; Mackwell, S. J.; Bell, D. R. Intercalibration of FTIR and SIMS for hydrogen measurements in glasses and nominally anhydrous minerals. Am. Mineral. **2007**, 92 (5–6), 811–828 DOI: 10.2138/am.2007.2248.

(78) Saito, M.; Marumo, K. Collagen cross-links as a determinant of bone quality: a possible explanation for bone fragility in aging, osteoporosis, and diabetes mellitus. Osteoporos. Int. **2010**, 21 (2), 195–214 DOI: 10.1007/s00198-009-1066-z.

(79) Weis, S. M.; Emery, J. L.; Becker, K. D.; McBride, D. J.; Omens, J. H.; McCulloch, A. D. Myocardial mechanics and collagen structure in the osteogenesis imperfecta murine (oim). Circ. Res. **2000**, 87 (8), 663–669.

(80) Paschalis, E. P.; Gamsjaeger, S.; Fratzl-Zelman, N.; Roschger, P.; Masic, A.; Brozek, W.; Hassler, N.; Glorieux, F. H.; Rauch, F.; Klaushofer, K.; et al. Evidence for a Role for Nanoporosity and Pyridinoline Content in Human Mild Osteogenesis Imperfecta. J. Bone Miner. Res. **2016**, 1–10 DOI: 10.1002/jbmr.2780.

For Table of Contents Use Only

Electron microscopy reveals structural and chemical changes at the nanometre scale in the osteogenesis imperfecta murine pathology

Authors:

Michał M. Kłosowski, Raffaella Carzaniga, Patricia Abellan, Quentin Ramasse, David W. McComb, Alexandra E. Porter, Sandra J. Shefelbine